Astron. Astrophys. 334, 71–86 (1998)

ASTRONOMY AND ASTROPHYSICS

An X-ray analysis of the cD cluster Abell 2199

Hassan Siddiqui[1,2], **G.C. Stewart**[2], **and R.M. Johnstone**[3]

[1] ESTEC, Astrophysics Division, Space Science Department, Postbus 299, 2200 AG Noordwijk, The Netherlands (hsiddiqu@astro.estec.esa.nl)
[2] Department of Physics and Astronomy, University of Leicester, University Road, Leicester LE1 7RH, UK
[3] Institute of Astronomy, Madingley Road, Cambridge CB3 OHA, UK

Received 1 October 1997 / Accepted 22 January 1998

Abstract. We describe the ROSAT analysis of the cD cluster Abell 2199. The spatial distribution is found to be slightly elongated, with an axis ratio of ≈ 0.8 and position angle of ≈ 45 degrees anticlockwise from due North about the cluster centre. The surface brightness profile reveals a significant cooling flow of $\approx 250\ \mathrm{M}_\odot\ \mathrm{yr}^{-1}$, although a lower mass deposition rate is deduced from the spectral data. The total gas and gravitational masses within a radius of 1.8 Mpc are found to be $\approx 1 \times 10^{14}\ \mathrm{M}_\odot$ and $\approx 5 \times 10^{14}\ \mathrm{M}_\odot$ respectively. The implications of these findings are discussed.

Key words: galaxies: clusters: individual: A 2199 – cooling flows – inter-galactic medium – dark matter – X-rays: galaxies – cosmology: observations

1. Introduction

Recent theories regarding cluster evolution suggest that they evolve through merging and once virialised, the central galaxy grows through 'dynamical cannibalism' as the central regions become denser (Sarazin 1986 and references therein). It is also plausible that the central galaxy evolves by the accretion of gas through a cooling flow. In this case, the gas could condense into a halo of low mass stars around the central galaxy. It has been suggested (Sarazin 1986) that cD clusters represent a relaxed stage of cluster evolution, especially if a strong cooling flow is present. Thus the gas mass distribution is expected to be of a smooth and spherical form.

Previous x-ray observations using Einstein and EXOSAT suggest that A2199 is a relaxed cluster. The Einstein Imaging Proportional Counter (IPC) observation of this cluster shows that it is approximately spherical, and optical data show the cluster to have a large cD galaxy (NGC 6166; $\alpha = 16^{\mathrm{h}}\ 28^{\mathrm{m}}\ 38.3^{\mathrm{s}},\ \delta = +39^\circ\ 33'\ 04.7''$) embedded in the central region. If A2199 is truly relaxed, then studies of the x-ray properties of this cluster would give important clues regarding its evolutionary path.

Abell 2199 is a moderately rich cluster, with an Abell richness class of 2 (Abell et al. 1989). Detailed optical studies have been made by Gregory & Thompson (1984) and Dixon et al. (1989). Zabludoff et al. (1990) obtained 71 redshifts for the cluster and find a mean z of 0.0309 and a velocity dispersion of $794\ \mathrm{km\ s}^{-1}$. The giant cD galaxy in the centre of the cluster, NGC 6166, which is associated with the radio source 3C 338, has also been studied in detail (Minkowski 1961 and references therein). Previous x-ray observations show that the cluster is moderately luminous in x-rays. The 2–10 keV flux of $\approx 7 \times 10^{-11}\ \mathrm{erg\ cm}^{-2}\ \mathrm{s}^{-1}$, which puts A2199 in the top 10 brightest clusters, corresponds to a luminosity of $3 \times 10^{44}\ \mathrm{erg\ s}^{-1}$ (Edge & Stewart 1991). A previous Ginga observation found the average gas temperature of the cluster to be $4.08\ \pm 0.08\ \mathrm{keV}$ (Butcher 1994) which is appropriate for a cluster of this luminosity (Edge & Stewart 1991).

A2199 is of particular interest for studies in the soft x-ray regime because it lies along a direction of extremely low galactic column density ($\mathrm{n_H} = 8.7 \times 10^{19}\ \mathrm{cm}^{-2}$). Previous studies using EXOSAT (Edge 1989), the EINSTEIN IPC (Stewart et al. 1984) and the ROSAT PSPC (Allen & Fabian 1997) have shown the cluster to have a cooling flow of approximately $80 - 200\ \mathrm{M}_\odot\ \mathrm{yr}^{-1}$. Spectral studies of the inner 0.05 degree region (160 kpc at the redshift of the cluster) with the EINSTEIN solid state spectrometer (SSS) show significant excess absorption in the x-ray spectra of A2199, of $1.4 \pm 0.2 \times 10^{21}\ \mathrm{cm}^{-2}$ (90 % confidence error; White et al. 1991), which suggests the presence of substantial quantities of cold gas within the cluster core.

This paper presents results from the ROSAT Position Sensitive Proportional Counter (PSPC; Pfeffermann et al. 1987) and Wide Field Camera (WFC; Wells et al. 1990). With its superior throughput, the PSPC allows a more sensitive investigation of the x-ray structure than the IPC and its energy bandpass is suited to the study of the cooling flow.

A2199 is unique in that, as shown in this paper, it is the only cluster so far to have been detected using the EUV-sensitive WFC. Such data is useful in examining the putative cold gas.

In this paper celestial positions are expressed in equatorial coordinates for the equinox 2000 unless otherwise stated.

Send offprint requests to: H. Siddiqui

2. Observation and data reduction

A ROSAT observation of Abell 2199 was performed on 1990 July 18 during the Performance Verification (PV) phase of the programme. The PSPC was the prime instrument. After excluding periods of high background from the PSPC data (master veto rates greater than $170\ \mathrm{ct\ s^{-1}}$, see Snowden et al. 1992 for details) an effective exposure time of 9260 sec was achieved with the PSPC. Fig. 1 shows a 0.1-2.0 keV PSPC image of the cluster smoothed using a Gaussian filter with a 30 arcsecond FWHM point spread function.

The extended emission due to the cluster is clearly seen. The cluster emission peaks at $\alpha = 16^{\mathrm{h}}\ 28^{\mathrm{m}}\ 39.0^{\mathrm{s}}$, $\delta = 39^{\circ}\ 32'\ 51''$, which is coincident with NGC 6166. The bright source ≈ 0.6 degrees to the North of A2199 is the AGN RX J16290 +4007, which is at a redshift of 0.272 (Giommi et al. 1991; Bade et al. 1992). An estimate of the background was obtained using an annulus between 0.75 and 0.85 degrees, which contains negligible cluster counts. Note that the nearby poor cluster, A2197, approximately 1.2 degrees North of NGC 6166, also has an insignificant contribution to the background counts. An estimate of the particle background over the region was made using the formulation of Plucinsky et al. (1993). The particle contribution is about 1.2 % of the total. The particle and residual (photon) background were corrected to the source region using the spatial form of Plucinsky et al. (1993) and the energy-dependent PSPC vignetting function respectively. In the case of spectral data, the corrected background was subtracted from the raw source spectra on a PHA channel-by-channel basis. For imaging data, each individual pixel was subtracted using the background over the appropriate energy range.

For the WFC, a total exposure time of 6283 sec was obtained with the S1a filter, and of 4540 sec with the S2b filter. The S1a and S2b filters have bandpasses at 10 % of peak of 90–210 eV and 62–111 eV respectively Briel et al. 1996. Fig. 2 shows the image obtained with the S1a filter of the WFC after smoothing with a 2.8 arcmin Gaussian.

The cluster emission is clearly visible. No significant detection of the cluster was made in the S2b band. The WFC data were corrected using a circular background of radius 0.25 degrees situated 0.8 degrees South of the cluster centre (and devoid of strong sources). The resultant count rate is $2.75\times10^{-2}\ \mathrm{ct\ s^{-1}}$ in the S1 band and a 1σ upper limit for the S2 band count rate of $1.2 \times 10^{-2}\ \mathrm{ct\ s^{-1}}$ was obtained.

3. Spectral analysis

For the purposes of detailed spectral analysis azimuthally binned spectra were extracted over 4 concentric annuli centred on the peak of the cluster x-ray emission. The radial extents were chosen so that the temperature and column density profiles could be resolved with as much spatial detail as possible, while ensuring good counting statistics. Table 1 lists the regions (labelled i–vi), plus 3 additional circular regions used to investigate the total cooling flow (v–vii).

For regions i–iv, the data were limited to channels 14-201. These were grouped to form 24 spectral bins of 8 PHA channels each, with the exception of Bin 1 which covered PHA channels 14-17. Over this range the calibration is reasonably well understood and afterpulse effects (Plucinsky et al. 1993) are minimised.

Table 1. The annuli used for spectral fitting. Count rates over PHA channels 14-201 are listed in column 4. 68 % confidence errors are quoted.

Region	**Inner Radius** arcmin	**Outer Radius** arcmin	**Count Rate** $\mathrm{ct\ s^{-1}}$
i	0	1	1.05 ± 0.01
ii	1	3	2.35 ± 0.02
iii	3	6	2.01 ± 0.02
iv	6	18	2.25 ± 0.02
v	0	3	3.40 ± 0.02
vi	0	6	5.41 ± 0.02
vii	0	18	7.63 ± 0.03

As Fig. 9 shows, cluster emission is apparent up to a detection limit of ≈ 0.7 degrees. Approximately 90% of the total cluster counts originate within Region vii, and the surface brightness is still sufficiently high to render systematic errors in the background estimation negligible. The hard x-ray spectrum obtained from the Ginga observation (Butcher 1994), over the energy range of 2 to 10 keV was used in combination with these data. The Ginga spectrum was corrected for position-dependant effects due to the collimator transmission by folding the surface brightness profile observed by the PSPC over a 2-d grid of measured collimator transmission. This yielded in an increase in the Ginga count rate of 25%. The PSPC dataset was renormalised by a factor of $+9.6\%$ to allow for the difference in spatial extents over which the PSPC and Ginga cluster data were accumulated.

The WFC data provides some spectral resolution at lower energies. The S1a background-subtracted count rates corresponding to regions v, vi and vii were combined with the PSPC data over these regions prior to fitting. The spectral range for the PSPC datasets in question was restricted to channels 18-201. The S2b background-subtracted count rate over 0.3 degrees was also included into the fitting process for region vii.

3.1. Single temperature models

The data were fitted to the optically thin plasma emission model of Raymond & Smith (1977), with photoelectric absorption along the line of sight (Morrison & McCammon 1983). The normalisation (emission measure) and temperature were allowed to vary. The redshift was fixed to the optical measurement of 0.0309 (Struble & Rood 1991). The hydrogen and helium abundances were set to the solar value. The low Z metal abundances were fixed at 0.30 solar with the exception of iron, which was fixed at the best fit value determined by Ginga of 0.26 solar (Butcher 1994). To examine the effect of soft x-ray absorption, two tests were conducted. In the first (Test A) the column density was fixed at the galactic value estimated from 21 cm observations of $8.7 \times 10^{19}\ \mathrm{cm^{-2}}$ (Stark et al. 1992). A sequence of trial fits was also performed in which the column density was

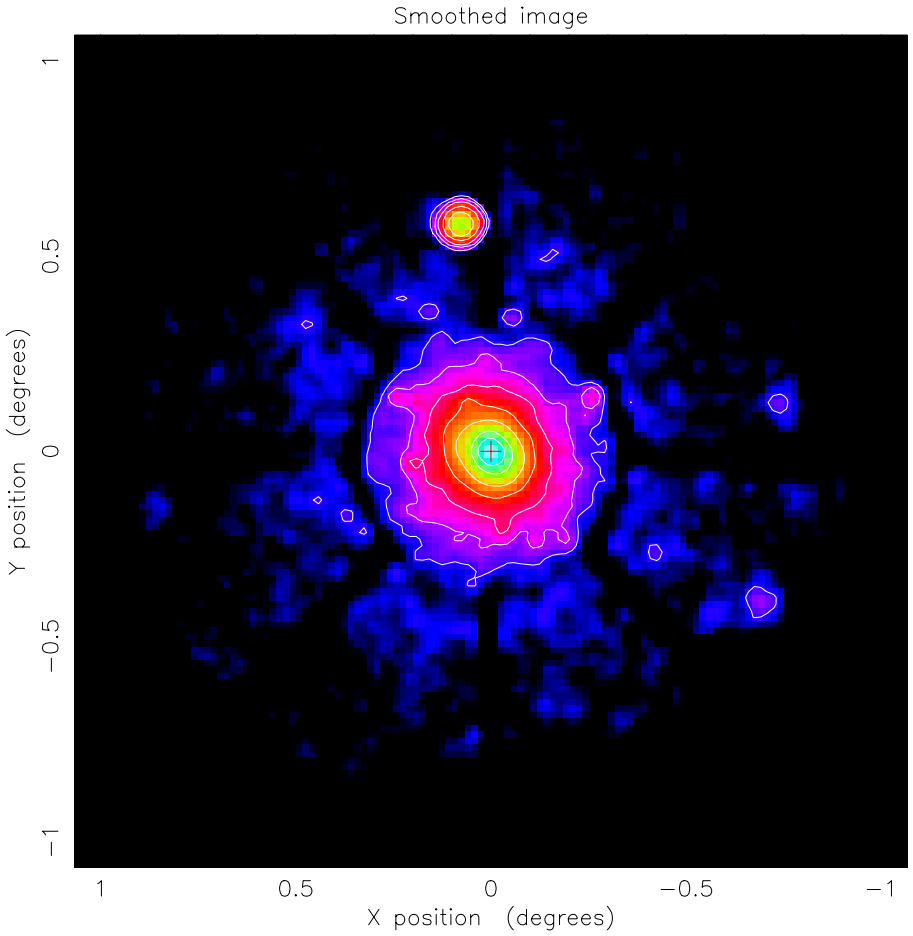

Fig. 1. A 0.1-2.0 keV raw PSPC contour image of A2199. A binsize of 30 arcseconds is used and the image is smoothed using a 1 arcminute Gaussian filter. The position of NGC 6166 is depicted as a red cross. Contours at intensities of 800, 150, 80, 30, 15 and 6 ct s^{-1} deg^{-2} are shown.

Table 2. For all annuli the number of degrees of freedom when the column density is fixed is 22 except for (vii) where it is 51. With the column density free this is reduced by 1.

	Test A		**Test B**		
Region	**Temperature** keV	χ^2	**Temperature** keV	**Column** $10^{21}\mathrm{cm}^{-2}$	χ^2
i	> 8.6	96.6	$2.8^{+0.8}_{-0.5}$	$0.126^{+0.010}_{-0.009}$	19.0
ii	$4.7^{+1.1}_{-0.8}$	29.0	$4.0^{+1.2}_{-0.8}$	$0.094^{+0.007}_{-0.007}$	23.9
iii	$5.8^{+1.5}_{-1.1}$	32.5	$4.7^{+1.9}_{-1.1}$	$0.094^{+0.008}_{-0.008}$	27.6
iv	$4.7^{+1.4}_{-0.9}$	41.5	$4.7^{+2.3}_{-1.1}$	$0.087^{+0.011}_{-0.013}$	41.5
v	$4.9^{+1.0}_{-0.7}$	75.2	$3.5^{+0.7}_{-0.5}$	$0.103^{+0.006}_{-0.006}$	31.8
vi	$5.2^{+0.8}_{-0.7}$	149.4	$3.9^{+0.5}_{-0.5}$	$0.101^{+0.005}_{-0.005}$	88.6
vii	$4.19^{+0.04}_{-0.04}$	135.4	$4.12^{+0.05}_{-0.05}$	$0.099^{+0.012}_{-0.012}$	70.1

allowed to vary as an adjustable parameter during fitting (Test B). Least squares fitting was performed, based on the χ^2 statistic described in Bevington & Robinson (1992). The results are summarised in Table 2.

The best fitting model to the joint PSPC/Ginga spectrum, in which the absorption is allowed to vary, is illustrated in Fig. 3.

The temperature and column density profiles derived by allowing the column density parameter to freely adjust are shown in Figs 4 and 5.

For the inner annuli, Test B yielded significantly improved fits. As shown in Fig. 5, this is due to the requirement of an excess column density within the central region while at radii greater than ≈ 54 kpc the measured values are consistent with the galactic 21 cm measurement. Inspection of the best fit residuals using an adjustable column density for regions v and vi show that they are dominated by large displacement of the S1 data point compared to the model ($\Delta\chi \approx 4$). This can be explained by poor calibration of the hard 'leak' at approximately 400 eV, which can have a strong effect on highly cut-off sources such as clusters.

The spectral data yielded a temperature profile (Fig 4) which is consistent with an isothermal value at radii greater ≈ 54 kpc, albeit poorly constrained at large radii.

The temperature is clearly lower in the innermost bin compared with the outer bins. As demonstrated later, deprojection of the surface brightness profile (see Sect. 4.4) shows that for any reasonable temperature profile the cooling time in the core of the cluster is much less than the Hubble time and therefore a cooling flow should be established. While this should mean that cooler x-ray emitting gas will be found at the cluster centre it does render the single temperature model invalid. To ascertain whether the inferred excess absorption is real the data over the central regions and that over the extent of the cluster have been compared against more complex models.

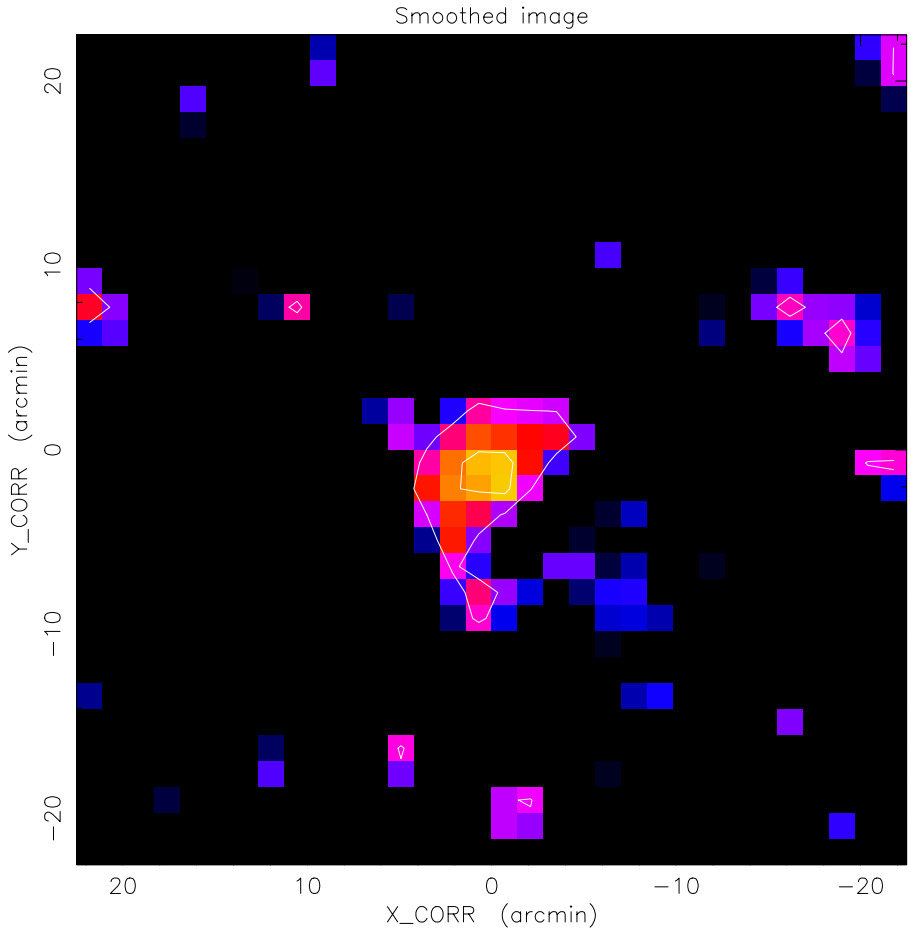

Fig. 2. A raw contour image of A2199 taken over the S1 band (90–210 eV). The data are constructed from 1.4 arcminute cells and smoothed using a 2.8 arcminute Gaussian filter. The contours shown correspond to 1.26 and 1.00 ct s^{-1} deg^{-2}.

3.2. Cooling flow model

The luminosity of a cooling flow in which there is no re-heating of the cooling gas is (Fabian 1991):

$$L_{cool} = \int_0^{T_{high}} EM(T)\Lambda(T)\, dT = \frac{5}{2}\,\frac{kT_{high}}{\mu\, m}\dot{M} \qquad (1)$$

where T_{high} is the temperature from which the gas is cooling, $EM(T)$ is its emission measure as a function of temperature, $\Lambda(T)$ is the cooling function and $\dot{M}$ is the mass deposition rate.

The cooling gas was modelled assuming a power law distribution of emission measure as a function of temperature, ie $EM(T) = EM_0\, T^n$. Note that for gas with a metal abundance of one-third solar at temperatures below ~ 2 keV $\Lambda(T) \propto T^0$, and hence is similar to the often-used XSPEC cooling model (Shafer et al. 1991). This was combined with a single temperature component to model gas beyond the cooling flow region. Trial fits using a model containing a single temperature and cooling flow component showed that both the isothermal temperature and the temperature from which the gas cools within the cooling flow were consistent at 4.2 keV . Both parameters were therefore fixed at this estimate. Note that this value is consistent with that found for the outer PSPC annuli. In practice, a lower temperature constraint of 0.1 keV was applied.

The results from these fits are summarised in Table 3. The mass deposition rates were computed from the predicted 0.1-10 keV flux of the cooling flow component, and a bolometric correction of 1.26 applied.

Table 3. The results for region (vii) are for 50(49) d.o.f.; all other fits are for 22(21) d.o.f.

Region	$\dot{\mathbf{M}}$ $\mathrm{M_\odot yr^{-1}}$	χ^2	$\dot{\mathbf{M}}$ $\mathrm{M_\odot yr^{-1}}$	**Column** $10^{21}\mathrm{cm^{-2}}$	χ^2
i	$0.0^{+5.9}_{-0.0}$	124.0	$7.6^{+9.3}_{-7.6}$	$0.123^{+0.010}_{-0.010}$	26.0
ii	$1.9^{+10.7}_{-1.9}$	30.6	$7.4^{+13.4}_{-7.4}$	$0.094^{+0.006}_{-0.006}$	21.8
v	$0.0^{+0.9}_{-0.0}$	79.3	$2.1^{+1.9}_{-1.9}$	$0.108^{+0.009}_{-0.007}$	29.2
vi	$5.6^{+16.2}_{-5.6}$	74.9	$19.3^{+21.2}_{-19.3}$	$0.101^{+0.004}_{-0.004}$	32.4
vii	$3.5^{+9.3}_{-3.5}$	100.1	$18.4^{+13.0}_{-12.6}$	$0.098^{+0.005}_{-0.005}$	67.7

Again the cases in which the absorption was fixed at the 21 cm value and where it was a free parameter were examined. Region iii, which encloses the outer region of the cooling flow is not included here as a preliminary spectral analysis showed it does not contain a significant cooling flow component, and so did not merit further consideration.

It was found that with this extra component included, excess absorption was still required in the inner regions, as was found in the SSS study of White et al. (1991). Note, however, that in their analysis an excess column density of $1.3 \pm 0.2 \times 10^{21}$ $\mathrm{cm^{-2}}$ is found within the inner 3 arcminute region of the cluster - much higher than the $\sim 4 \times 10^{19}$ $\mathrm{cm^{-2}}$ found here. This discrepancy

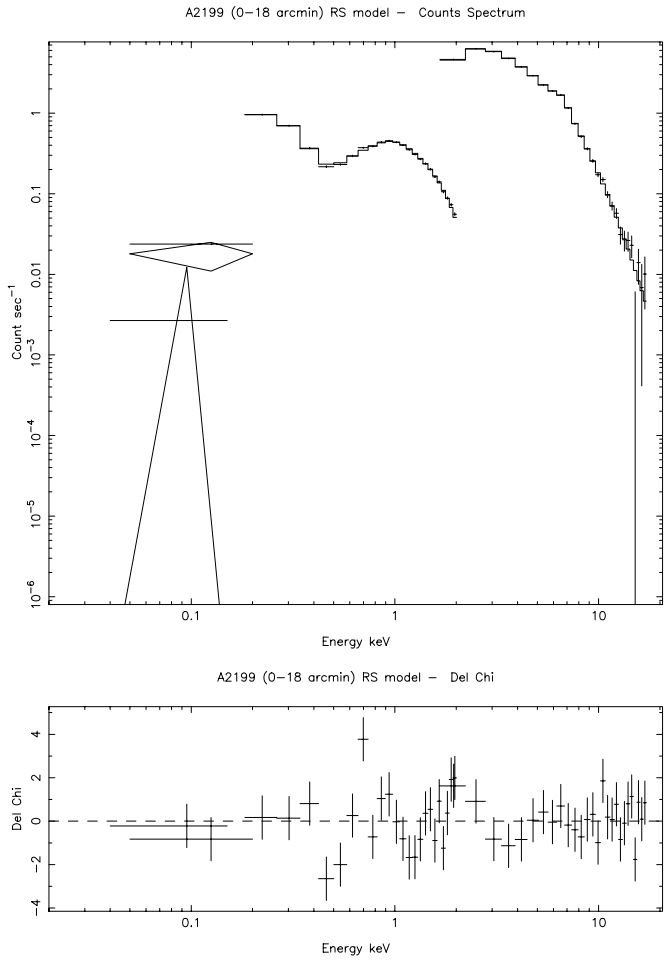

Fig. 3. The best fitting single temperature model to region vii. The absorption was a free parameter during the fitting process. The lower panel shows the $\Delta\chi$ residuals yielded from the fit.

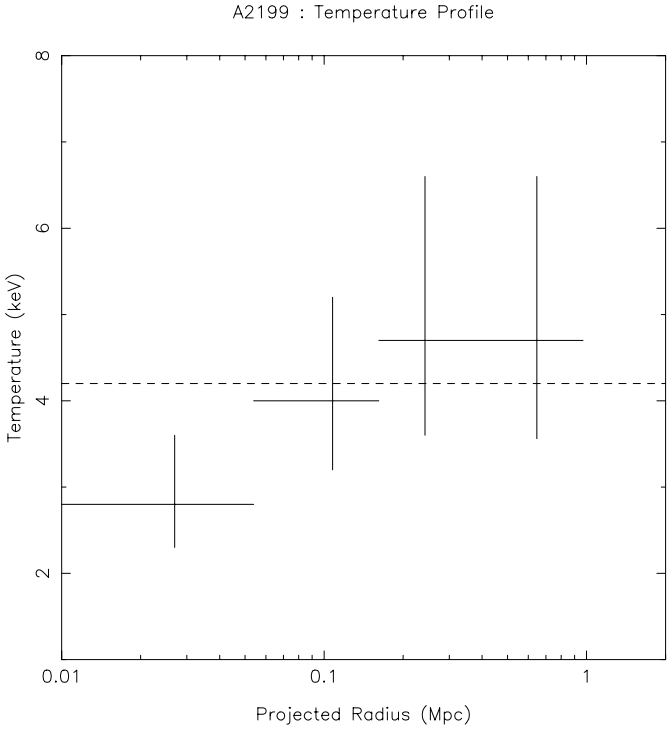

Fig. 4. The cluster temperature profile derived from spectral fitting of concentric regions about the x-ray centre. The dashed line shows the best fit temperature using Ginga alone, of 4.08 keV. A clear positive slope within a projected radius of 0.16 Mpc can be seen.

Table 4. The result for Region (vii) is for 48 d.o.f.; all other fits are for 20 d.o.f.

Region	$\dot{\mathbf{M}}$ $\mathrm{M_\odot yr^{-1}}$	**Intrinsic Column** $10^{21}\mathrm{cm^{-2}}$	**Covering Fraction**	χ^2
i	$22.8^{+26.5}_{-6.6}$	$1.72^{+2.38}_{-0.51}$	$1.00^{+0.00}_{-0.28}$	28.1
ii	$9.5^{+83.8}_{-9.3}$	$0.30^{+16.47}_{-0.30}$	$0.88^{+0.12}_{-0.62}$	22.9
v	$23.4^{+70.3}_{-7.9}$	$0.32^{+6.97}_{-0.15}$	$1.00^{+0.00}_{-0.47}$	40.6
vi	$31.6^{+94.6}_{-14.9}$	$0.84^{+5.83}_{-0.38}$	$0.93^{+0.07}_{-0.42}$	37.0
vii	$58.5^{+66.2}_{-14.9}$	$2.46^{+4.50}_{-1.77}$	$1.00^{+0.00}_{-0.24}$	65.7

suggests that the absorber only partially covers the source, and, because it is only required in the central regions is probably associated with the cluster core itself.

The mass deposition rates yielded are clearly very low (indeed the SSS estimate for the mass deposition rate within the inner 3 arcminutes is 60^{+20}_{-17} $\mathrm{M_\odot\ yr^{-1}}$; White et al. 1991), and may be a consequence of the competition between the normalisation of the isothermal component and that of the cooling flow component. An estimate for the isothermal flux within regions v and vi was ascertained by fitting the Ginga spectrum to an isothermal model. The original Ginga spectrum was again corrected for the difference in extents over which these data and the PSPC data in question was accumulated: the appropriate correction factors for regions v and vi were ≈ 0.35 and ≈ 0.6 respectively. Fitting region v to a cooling flow model using an isothermal normalisation fixed at the scaled-down Ginga estimate, and a fixed intrinsic column density of 1.4×10^{21} $\mathrm{cm^{-2}}$ above the galactic value yielded a mass deposition rate of $61.8^{+3.9}_{-3.9}$ $\mathrm{M_\odot\ yr^{-1}}$, in excellent agreement with the SSS findings, although the best fit χ^2 was 147.1 for 23 d.o.f - the residuals to this fit show that this can be explained by excess flux below ≈ 0.6 keV (outside the energy range of the SSS) and indicate the requirement for a low covering fraction. Repeating the same procedure for region vi, but using a column density fixed at the galactic value yielded a mass deposition rate of 40.2 $\mathrm{M_\odot\ yr^{-1}}$ ($\chi^2 = 96.6$ for 23 d.o.f). Allowing the column density to vary gives an $\dot{\mathrm{M}}$ of 49.9 $\mathrm{M_\odot\ yr^{-1}}$ and a best fit column density of $1.00^{+0.04}_{-0.04} \times 10^{20}$ $\mathrm{cm^{-2}}$ ($\chi^2 = 43.4$ for 22 d.o.f).

3.3. The effect of partial covering

A partial covering screen was incorporated into the cooling flow model such that a fraction of the cooling flow was obscured by an intrinsic absorber, whilst the remainder was affected only by the galactic column density. The fraction was adjusted during the fitting process as a free parameter. The results of this model are summarised in Table 4.

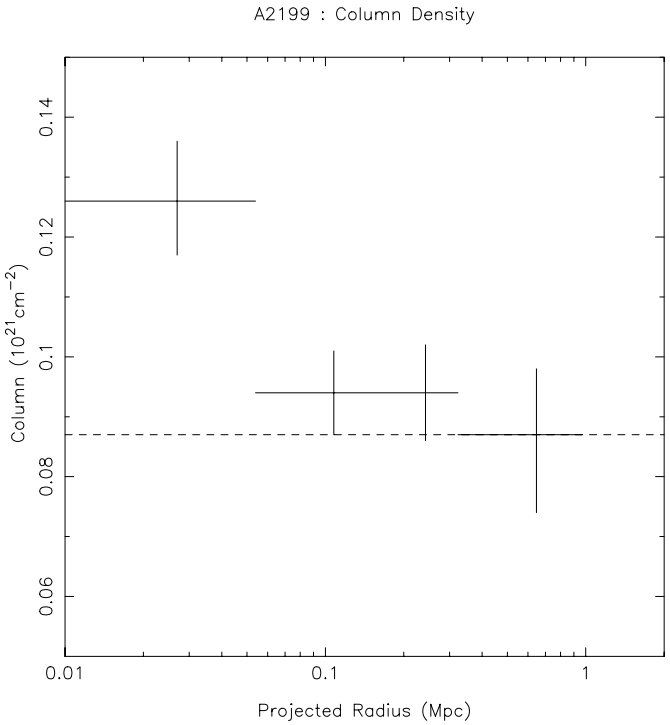

Fig. 5. The best fitting column density as a function of radius. Beyond 0.16 Mpc the derived column density is consistent with the galactic value. Note the increase in column density towards the cluster centre.

Table 5. The result for Region (vii) is for 48 d.o.f.; all other fits are for 20 d.o.f. The errors for regions v - vii are 68 % confidence estimates for two parameters of interest.

Region	$\dot{\mathbf{M}}$ $\mathrm{M_\odot yr^{-1}}$	**Intrinsic Column** $10^{21}\mathrm{cm^{-2}}$	**Covering Fraction**	χ^2
i	$8.3^{+10.0}_{-8.3}$	$0.08^{+0.89}_{-0.03}$	$1.00^{+0.00}_{-0.66}$	26.6
ii	$7.7^{+59.3}_{-7.7}$	$0.35^{+17.36}_{-0.35}$	$0.11^{+0.89}_{-0.01}$	23.3
v	$5.0^{+1.8}_{-2.9}$	$1.46^{+2.10}_{-0.65}$	$0.37^{+0.63}_{-0.20}$	40.6
vi	$21.3^{+13.1}_{-15.1}$	$0.03^{+0.05}_{-0.01}$	$1.00^{+0.00}_{-0.69}$	31.3
vii	$13.4^{+9.6}_{-6.9}$	$1.73^{+0.80}_{-0.87}$	$0.38^{+0.16}_{-0.12}$	63.0

This gave a marginally better fit than the cooling flow model with variable absorption. In general, an intrinsic column density of between 0.3 and 3.5×10^{21} cm^{-2} was measured, and mass deposition rates $10 - 60$ M$_\odot$ yr^{-1} were found.

However, this model does not account for the emission from the isothermal phase obscured by this absorbing screen. Correcting for this yields the results shown in Table 5.

The error ranges for regions v - vii were computed at the 68 percent confidence level for 2 parameters of interest ($\Delta\chi^2 = 2.28$) as this approach provides informative constraints on the covering fraction and intrinsic column density. The best fit model to region vii is shown in Fig 6.

In this model, a range in intrinsic column density of $(0.08 - 1.73) \times 10^{21}$ cm^{-2} was found. However, this model also gives in general very low mass deposition rates. To examine whether this is a cause of competition between isothermal and cooling flow components, the fit to region v is repeated with the isothermal component fixed at the value estimated from the joint PSPC/Ginga spectrum (Fig. 7).

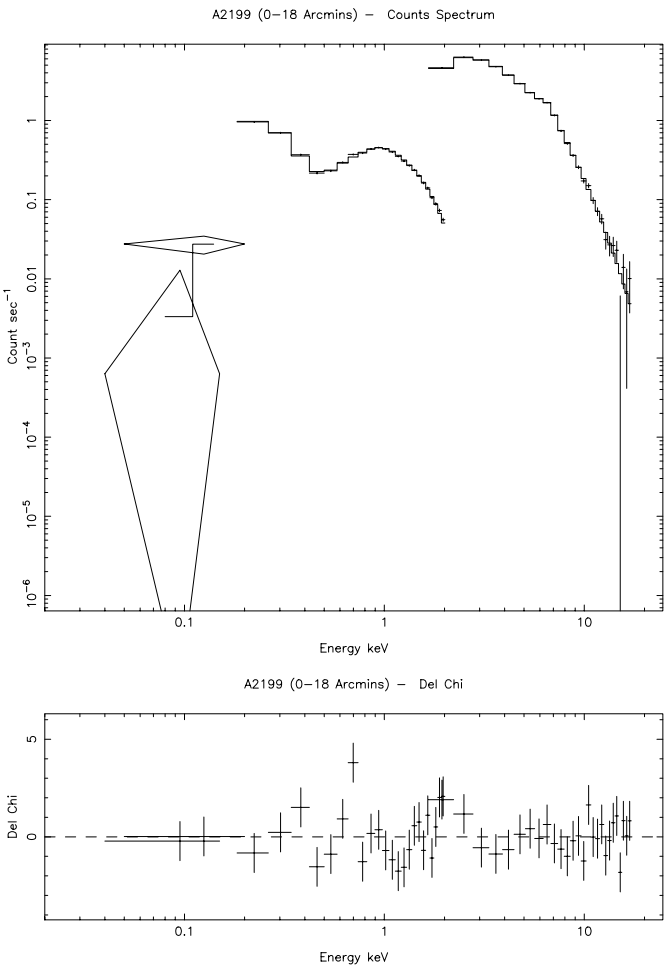

Fig. 6. The best fitting modified covering fraction model to region vii.

This gives a best estimate for $\dot{\mathrm{M}}$ of $66.9^{+3.8}_{-6.9}$ M$_\odot$ yr^{-1}, with an intrinsic column of $3.5^{+3.7}_{-2.0} \times 10^{21}$ cm^{-2}, and a covering fraction of $0.29^{+0.09}_{-0.09}$ ($\chi^2 = 54.0$ for 21 d.o.f.; the errors quoted correspond to the 68 % confidence level for 2 parameters of interest). Consistent results are found after applying the above procedure to region vi. These are generally in good agreement with the findings of Allen & Fabian (1997). These results suggest that the cluster contains an intrinsic, partially covering screen. The models were introduced in order of their 'physical plausiblity'. However, this sequence has not necessarily resulted in an improvement in the goodness of fit. Analysis of high quality data expected from missions such as ASCA, AXAF or XMM would be required to provide a clear understanding of the nature of this intrinsic absorber. A similar effect has been noted in a PSPC observation of the A2142 cluster by Siddiqui *et al.* (in preparation), in which an intrinsic column density of 10^{20} cm^{-2} and a covering fraction of roughly 0.9 were found.

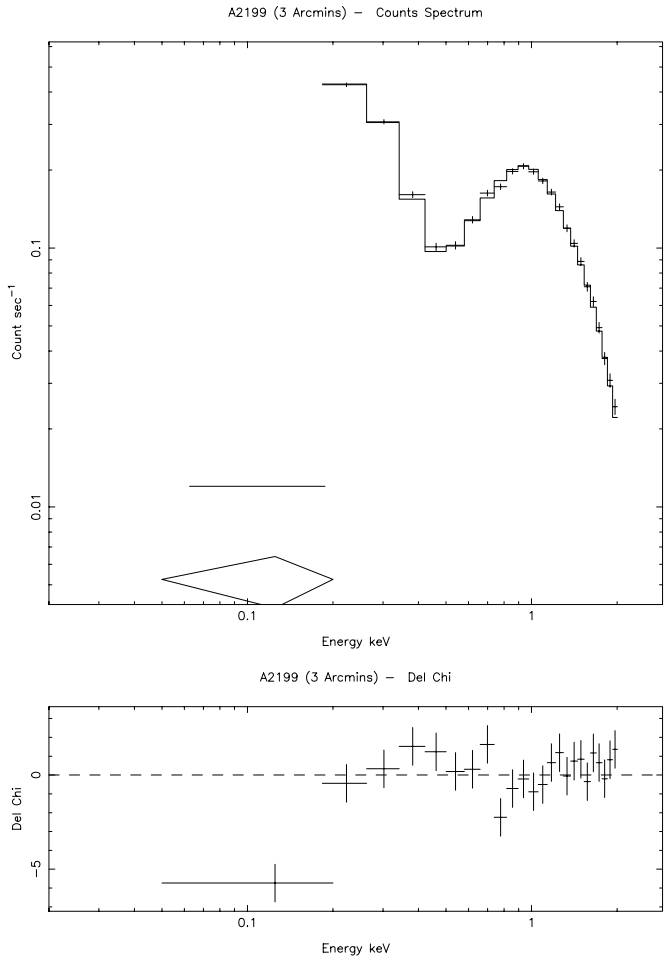

Fig. 7. The best fitting modified covering fraction model to region v, assuming a isothermal component fixed at the scaled PSPC/Ginga estimate.

4. Spatial analysis

4.1. The cluster morphology

In order to view the x-ray emission of the cluster, a 2×2 degree image of the cluster was constructed. A binsize of 30 arcsec was used, and the data were restricted to a spectral range corresponding to PHA channels 10-200 . As can be seen from Fig. 1 the gas distribution is slightly elliptical.

Contour analysis was performed on the images using the RGASP package (Davis 1991). Starting from the cluster centre and stepping outwards, the routine fits ellipses to contours of constant surface brightness. For each trial fit, the variation in the pixel intensity around the ellipse gauges the necessary adjustments to the fit parameters, e.g. a first order variation indicates an error in the x-y position, while a non-zero value in the second order sine and cosine components necessitates changes in position angle and ellipticity. These parameters are adjusted until the variation in the pixel intensity is minimised. Table 6 shows the results obtained from the isophotal analysis of the cluster emission. These results are shown pictorially in Fig. 8.

There is a tentative suggestion for substructure within the inner regions. At radii of less than 0.06 deg (200 kpc), the centroid of the fitted ellipses changes in a South-West direction, parallel with the major axis of the cluster. Moreover, the plot of the recombined ellipses shows some distortion at ≈ 0.04 degrees (120 kpc) SW of the centre, suggesting substructure at this position. Beyond 0.07 degrees the elongation and position angle are reasonably stable, and have values of 0.82 ± 0.03 and 45 ± 15 deg respectively (the errors here correspond to the scatter in the plots). The position angle is coincident with that for the major axis of the cD galaxy (31 ± 1 degrees; Porter et al. 1991). and for the galaxy distribution (≈ 35 degrees; Dixon et al. 1989).

4.2. The surface brightness profile

The azimuthally averaged surface brightness profile of the cluster x-ray emission after subtraction of the background is shown in Fig. 9.

A significant detection of the cluster emission is still evident out to an angular radius of 0.6° which is equivalent to 1.8 Mpc from the x-ray centre. To parameterise the surface brightness profile the following function is used (see Cavaliere & Fusco-Femiano 1976):

$$I(\theta) = I_0 \left(1 + \left(\frac{\theta}{a}\right)^2\right)^{\frac{1}{2}-3\beta} \quad (2)$$

Where θ is the projected radius, a is the core radius, and β is the ratio of scale heights of the gas and galaxies. No acceptable fit to the full distribution could be found. Following the example of Jones & Forman (1984), analysis was restricted to data between 0.1 degrees (0.32 Mpc) and 0.3 degrees (1 Mpc). The lower limit is used to exclude emission from a central cooling flow. This gave best-fitting values for the core radius and β of 120^{+45}_{-36} kpc and 0.62 ± 0.05 respectively, with a χ^2 value of 68 for 55 degrees of freedom. These values are consistent with the ranges obtained from the analysis of the EINSTEIN IPC data by Forman et al. (1984) (a=120-160 kpc; $\beta = 0.63 - 0.73$). It is noted, however, that Gerbal et al. (1992) find much smaller values from their analysis of IPC data (their upper limits are $\mathrm{a} \approx 37$ kpc and $\beta \approx 0.44$. It is not obvious what is the cause of this descrepancy. Fig. 9 shows a significant excess above this model within 0.1 degrees.[1] This is characteristic of clusters which have cooling flows (Fabian 1991).

[1] A 50 ks PSPC observation of this cluster had been performed during 1993 Jul 26-28. A King fit to the surface brightness profile obtained from these data over the full PSPC band over the radial ranges between 0.04 and 0.24 degrees and 0.55-0.78 degrees gives a best fit core radius and β of $113.9^{+5.9}_{-5.0}$ kpc and $0.62^{+0.01}_{-0.01}$ respectively (Pownall 1994 private communication). These are in agreement with the shorter observation described above, and much better constrained than the IPC data. The goodness of fit yielded is poor ($\chi^2 = 117$ for 48 degrees of freedom). Given the high statistical quality of the data, this result calls into question the validity of the King approximation.

Table 6. Results from the isophotal analysis. Columns 2–8 show for each ellipse its intensity (column 1), semi-major axis, semi-minor axis, elongation, position angle (Anticlockwise from North), x-centroid shift (+ve = due East) and y-centroid shift (+ve = due North) respectively.

Ellipse	**Intensity** $\mathrm{ct\ s^{-1}\ deg^{-2}}$	**a** deg	**b** deg	**b/a**	**PA** deg	**Δx** deg	**Δy** deg
1	1962.60	4.17E-03	3.75E-03	0.90	90.0	0.00E+00	0.00E+00
2	1906.33	4.59E-03	4.09E-03	0.89	44.0	0.00E+00	8.35E-05
3	1840.69	5.05E-03	4.50E-03	0.89	42.0	0.00E+00	1.25E-04
4	1770.08	5.55E-03	4.92E-03	0.89	40.0	0.00E+00	2.09E-04
5	1699.09	6.09E-03	5.38E-03	0.88	39.0	0.00E+00	2.50E-04
6	1626.80	6.71E-03	5.84E-03	0.87	36.0	4.17E-05	2.92E-04
7	1574.70	7.38E-03	6.17E-03	0.84	31.0	8.35E-05	4.17E-04
8	1530.98	8.13E-03	6.46E-03	0.79	27.0	1.67E-04	5.84E-04
9	1485.08	8.92E-03	6.76E-03	0.76	25.0	2.09E-04	6.67E-04
10	1431.05	9.84E-03	7.13E-03	0.72	22.5	2.50E-04	7.51E-04
11	1370.94	1.08E-02	7.59E-03	0.70	20.5	2.50E-04	7.51E-04
12	1278.47	1.19E-02	8.38E-03	0.71	19.0	2.50E-04	5.84E-04
13	1167.05	1.31E-02	9.51E-03	0.73	16.0	3.34E-04	4.59E-04
14	1041.79	1.44E-02	1.14E-02	0.79	11.0	9.59E-04	2.92E-04
15	936.40	1.58E-02	1.33E-02	0.84	10.0	1.42E-03	1.25E-04
16	873.30	1.74E-02	1.44E-02	0.83	17.8	1.21E-03	0.00E+00
17	832.56	1.91E-02	1.51E-02	0.79	25.8	6.26E-04	-5.00E-04
18	767.91	2.11E-02	1.62E-02	0.77	28.8	2.09E-04	-6.25E-04
19	679.60	2.32E-02	1.83E-02	0.79	31.8	-3.34E-04	-5.84E-04
20	596.75	2.55E-02	2.07E-02	0.81	39.2	-7.09E-04	-6.25E-04
21	515.40	2.81E-02	2.31E-02	0.82	40.2	-6.25E-04	-7.09E-04
22	461.74	3.09E-02	2.52E-02	0.82	36.2	-9.17E-04	-1.58E-03
23	397.77	3.39E-02	2.81E-02	0.83	31.2	-1.54E-03	-1.63E-03
24	337.66	3.73E-02	3.11E-02	0.83	30.8	-2.71E-03	-2.38E-03
25	304.18	4.11E-02	3.32E-02	0.81	38.8	-4.55E-03	-3.92E-03
26	267.54	4.52E-02	3.60E-02	0.80	30.8	-3.75E-03	-3.79E-03
27	233.51	4.97E-02	3.96E-02	0.80	23.8	-3.75E-03	-3.79E-03
28	203.70	5.47E-02	4.28E-02	0.78	32.2	-5.09E-03	-5.05E-03
29	165.88	6.01E-02	4.85E-02	0.81	38.2	-5.63E-03	-5.80E-03
30	130.60	6.61E-02	5.54E-02	0.84	40.2	-4.80E-03	-4.30E-03
31	111.60	7.28E-02	5.80E-02	0.80	37.2	-3.88E-03	-4.46E-03
32	94.65	8.00E-02	6.62E-02	0.83	44.2	-2.46E-03	-4.50E-03
33	82.04	8.80E-02	7.11E-02	0.81	51.2	1.83E-03	-5.17E-03
34	59.81	9.69E-02	8.11E-02	0.84	58.2	2.92E-03	-4.30E-03
35	48.88	1.07E-01	8.71E-02	0.82	50.2	3.09E-03	-1.67E-03
36	41.36	1.17E-01	9.58E-02	0.82	50.2	5.84E-03	2.50E-03
37	33.78	1.29E-01	1.04E-01	0.81	38.2	5.13E-03	5.96E-03
38	28.01	1.42E-01	1.14E-01	0.81	32.2	7.84E-03	5.09E-03
39	20.87	1.56E-01	1.27E-01	0.82	43.8	7.76E-03	1.63E-03
40	18.01	1.72E-01	1.44E-01	0.84	43.8	1.13E-02	-5.00E-04
41	15.46	1.89E-01	1.66E-01	0.88	35.8	1.11E-02	-4.71E-03
42	13.66	2.08E-01	1.82E-01	0.87	31.8	2.00E-02	-8.01E-03
43	13.91	2.28E-01	1.77E-01	0.77	43.8	1.77E-02	-6.00E-03

The emission profile obtained from the S1a filter of the WFC, constructed using 2 arcmin radial bins was also examined using the same model (see Fig. 10).

This gave a best fit core radius of 118^{+742}_{-118} kpc and scale height β of $0.6^{+1.2}_{-0.2}$ ($\chi^2 = 9.5$ for 13 degrees of freedom). The cooling flow region was included in the fitting process due to the limited number of data points. The values for the core radius and slope measured are therefore under- and over-estimates respectively of the true King parameters.

4.3. Softness ratio

A useful means of determining the uniformity of the cluster gas is by use of softness ratios. These were constructed as a basic means of mapping the cluster temperature out to $\approx 0.6^{\circ}$ (1.8 Mpc). The spectral bands correspond roughly to the energy ranges of 0.1-0.5 keV (the 'soft' band), 0.5-1 keV (medium) and 1-2 keV (hard). To ensure good statistics for radii greater than 0.2 degrees (646 kpc), the original surface brightness profiles were rebinned using variable bin sizes before the ratios were

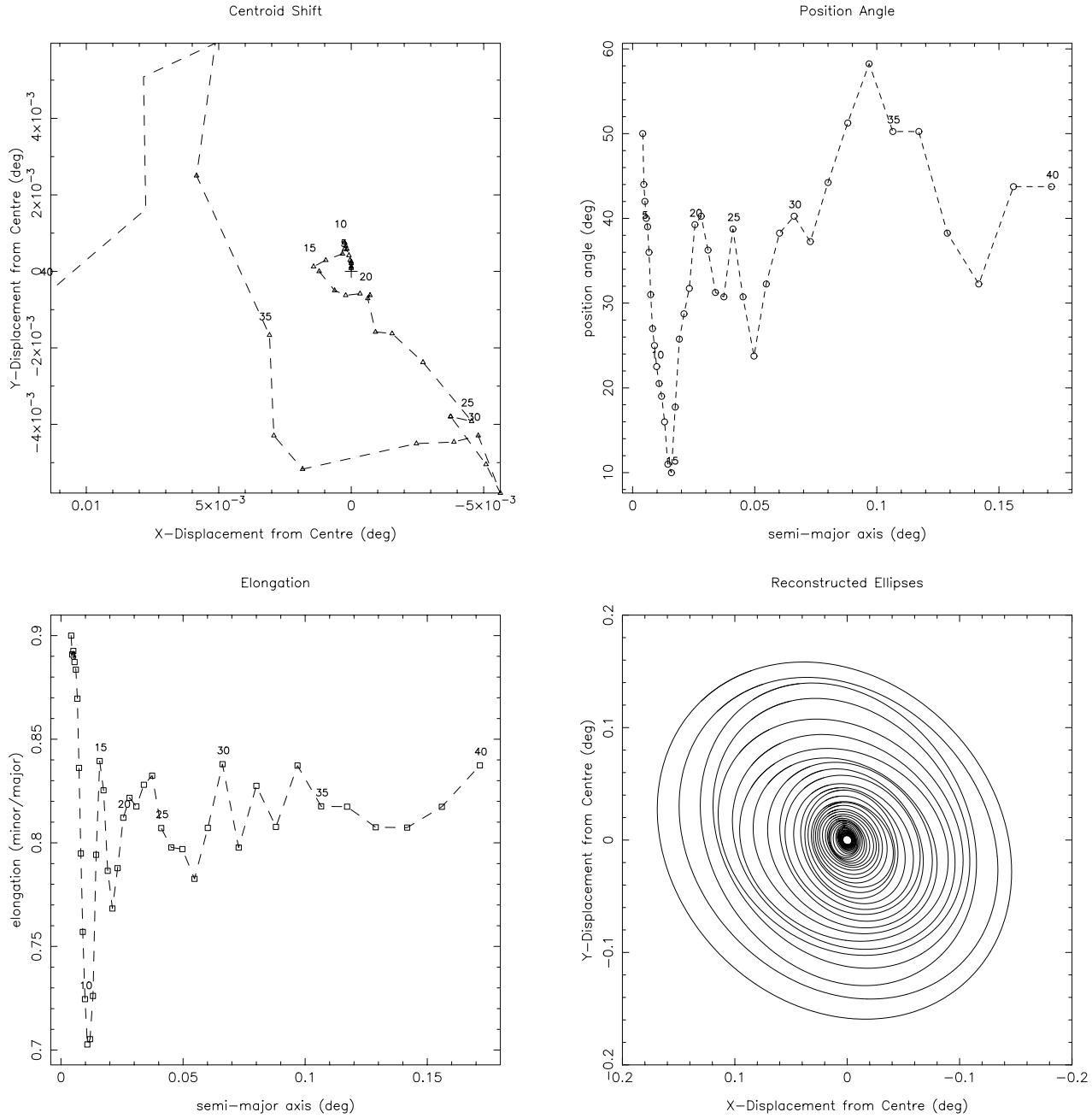

Fig. 8. The morphological properties of the cluster determined using the RGASP isophotal analysis technique. The top–left plot shows the centroid position of each ellipse with respect to the x-ray centre of the cluster. The top–right and bottom–left plots show the variation of position angle and elongation as a function of semi-major axis, while the final diagram shows a reconstruction of the fitted ellipses.

calculated. The radial variation of the soft and hand band ratio is shown in Fig. 11. The radial variations of the soft–medium, and medium–hard show similar behaviour.

The cluster spectrum clearly hardens with decreasing radius within 160 kpc, which is surprising considering the temperature gradient noted in Sect. 3. This can be explained in terms of the excess absorption, which is apparent over the same radius as the hardening, and increases towards lower radii. Between 160 and 600 kpc the ratios are fairly constant suggesting that the gas is isothermal. At radii greater than 600 kpc, there is a tentative suggestion of slightly cooler cluster emission, but the ratios are poorly constrained over this region.

4.4. Deprojection results

The deprojection technique described in Fabian et al. (1981) was used to determine various cluster gas properties as a function of radius. Constraints on the gravitational mass were obtained by utilising a variety of gravitational potentials. The temperature profiles obtained from each deprojection run were ‘re-projected’

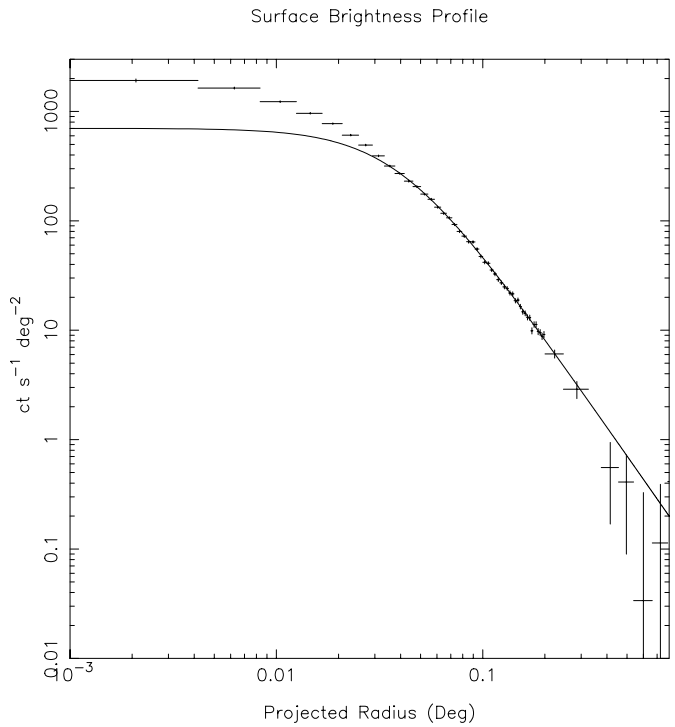

Fig. 9. The 0.1–2.0 keV surface brightness profile (background subtracted and devignetted). The solid curve depicts the best fit King profile. The central excess characteristic of a cooling flow can be clearly seen.

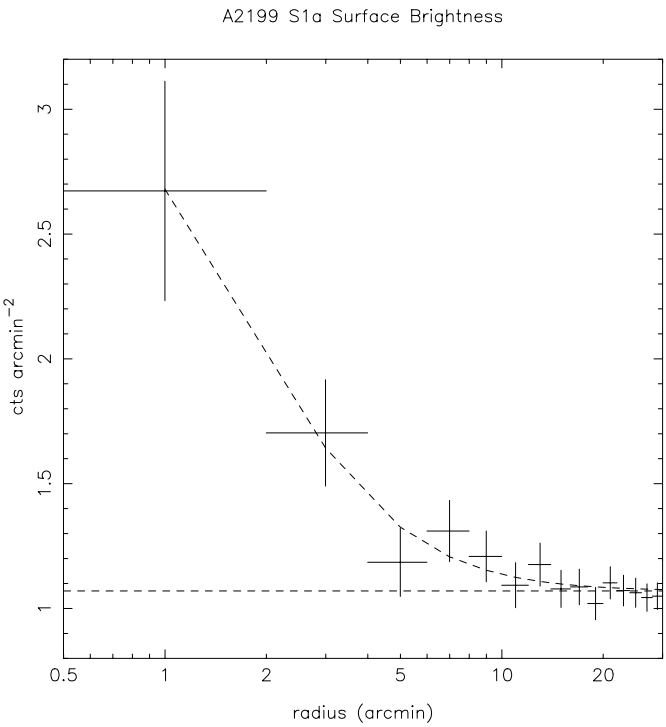

Fig. 10. The raw surface brightness profile of A2199 using the WFC S1 filter, in units of $\mathrm{ct\ arcmin^{-2}}$ (note the S1 exposure time is 6283 sec). The best fit King profile and background are shown as dashed lines.

Table 7. The trial gravitational potentials used during the deprojection analysis.

Model	Shape	Parameters
A	King (Optimum)	$\sigma_{\rm v} = 700\ \mathrm{km\ s^{-1}}$; core = 0.15 Mpc
B	King (Minimum)	$\sigma_{\rm v} = 650\ \mathrm{km\ s^{-1}}$; core = 0.17 Mpc
C	King (Maximum)	$\sigma_{\rm v} = 875\ \mathrm{km\ s^{-1}}$; core = 0.18 Mpc
D	Linear	Gradient = $2.75 \times 10^8 \odot\ \mathrm{pc^{-1}}$
E	de Vaucouleurs	$\sigma_{\rm v} = 700\ \mathrm{km\ s^{-1}}$; eff. radius = 3 Mpc

and compared to the spectral data. To re-project a profile, the temperature in each individual shell was weighted by the appropriate emission measure, and summed along the line of sight. A summary of the trial models and their parameters are shown in Table 7. A galactic column density was assumed throughout this analysis.

The gas density solution (Fig. 12) was very stable to the choice of potential ($\Delta\rho \propto \Delta \mathrm{T}^{0.25}$). The density peaks at $1.5 \times 10^{-2}\ \mathrm{cm^{-3}}$ within the central 50 kpc bin.

The deprojected temperature profiles yielded from this analysis are shown in Fig. 13.

All of these profiles are compatible with the spectral result, with the exception of the Linear model (D), which overestimates the temperature at lower radii. The de Vaucouleurs model (E) imposes a temperature within the bounds estimated by the King profiles. The re-projected temperature constraints determined from the King potentials are in good agreement with the spectral measurements and are shown in Fig. 14.

While it can be seen that a range of trial potentials is consistent with the observations, the optimum is close to that of model B. This model assumes a velocity dispersion of $700\ \mathrm{km\ s^{-1}}$ which is in good agreement with the observed value of $794\ \mathrm{km\ s^{-1}}$ (Zabludoff et al. 1990). This consistency suggests that the level of substructure of A2199 is very low.

4.4.1. Mass deposition rate

The variation in cooling time and mass deposition rate profiles as a function of radius are shown in Fig. 12. Within a radius of $250\ \mathrm{kpc}$, the cooling time is less than $2 \times 10^{10}\ \mathrm{yr}$. The mass deposition rate within this radius is $200 - 280\ \mathrm{M_\odot\ yr^{-1}}$. Consistent results were also obtained on re-analysis of the Einstein IPC and HRI datasets. The spectral estimate for the mass deposition rate assuming no intrinsic absorption is $40\ \mathrm{M_\odot\ yr^{-1}}$, from the fit to region vi using a fixed isothermal component. This value is much lower than that derived from deprojection. Using the results from the Einstein HRI deprojection analysis to trace the mass deposition rate and cooling time within 100 kpc, it was found that these differing estimates can be reconciled if the cooling radius is lowered to 40 kpc, which means a cooling flow age of approximately 2×10^9 yr. In the hierarchical merging scheme this would mean that a recent merger, 2 billion years ago, disrupted a previous cooling flow. The strength of the present cooling flow thus reflects the epoch of this merger. Assuming no further hindrance, the cooling flow will strengthen to $\approx\ 250\ \mathrm{M_\odot\ yr^{-1}}$ within the next Hubble time. A similar

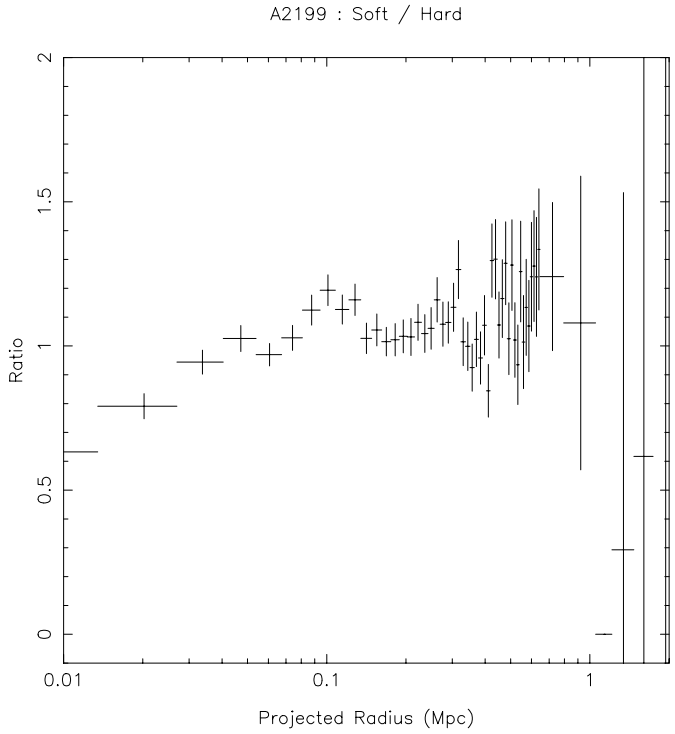

Fig. 11. The 'soft-hard' ratio as a function of radial distance.

descrepancy was found in A2142 by Siddiqui et al. (in preparation) and Siddiqui (1995), and by Allen & Fabian (1997) in their study of a sample of clusters observed by the PSPC, which included A2199.

4.4.2. Gas and gravitational mass profiles

As shown in Table 7, a range of core radii of 0.15 to 0.18 Mpc are allowed by the PSPC data. Using the constraints of the re-projected temperature distributions, limits can be established on the allowed gravitational potential at any given radius, and hence on the total mass distribution within the cluster. Fig. 15 shows the gravitational mass profiles corresponding to each trial model. Again, the Linear model produces a high central mass which is clearly incompatible with the spectral data. The constraints provided by the PSPC data limit the total mass within 1.8 Mpc to $3 - 6 \times 10^{14}$ $\odot$. (Note that the lower limit allows a cooler outer cluster halo).

The total gas mass within this radius is $\approx 10^{14}$ $\odot$. Both gas and gravitational mass distributions are in good agreement with Einstein IPC studies of the same cluster (Gerbal et al. 1992) and with the spatial analysis of the PSPC data performed by Buote & Canizares (1996). Using the King models combined with the density profile, limits to the gas fraction can be obtained (fig 16). At a radius of 1.8 Mpc, this is found to lie between 10 and 30 %, similar to that found in recent observations of other clusters (e.g. White et al. 1993; White 1994).

5. Discussion

5.1. The X-ray structure

The PSPC imaging data of the cluster show a distinct elongation of the cluster gas along a NE-SW direction. The orientations of the cluster gas, galaxy distribution and central galaxy are consistent with one another suggesting that both the gas and galaxy distributions follow the same underlying potential. This demonstrates a unique coherence over a large range of scales. The isophotal analysis reveals a slightly elongated structure parallel with the major axis of the cluster, suggesting that A2199 possesses some substructure.

5.2. Cold gas within the cluster

The combined WFC-PSPC-Ginga spectral fits presented in Sect. 3.3 suggest that a model in which the central regions of A2199 are covered by a cold absorbing medium is compatible with the observations. It is becoming increasingly evident that a centralised, intrinsic column density is a common feature in many rich clusters, as demonstrated by EINSTEIN SSS studies (White et al. 1991) and a ROSAT study of the Centaurus cluster (Allen & Fabian 1994). Within the inner 3 arcminute region of the cluster, an intrinsic column density of 3.5×10^{21} cm^{-2} with a partial covering fraction of 0.28 is found. The mass of cold gas, M_{cold} over the cooling radius of $\mathrm{R} = 40$ kpc can be estimated from the following equation:

$$M_{cold} = 1.36\ m_H \pi\ R^2\ \Delta n_H\ F_{cov} \quad (3)$$

where R is the radius of the absorbing screen, m_H is the mass of a hydrogen atom, 1.36 corresponds to the mean atomic weight per hydrogen atom and F_{cov} is the covering fraction. The intrinsic column density then corresponds to approximately 5×10^{10} M$_\odot$ of cold gas.

It is possible that a high metal content associated with the central regions might mimic the effect of extra absorption. Allen et al. (1993) have rejected this hypothesis for A478, but a high metal content is found to produce similar results to photoelectric absorption in the Centaurus cluster (Allen & Fabian 1994). This effect is tested in A2199 by stepping through a range in metal abundances from 0.1 to 0.6 solar, the latter corresponding to twice the large-beam Ginga estimation. Using abundances other than the nominal value of 0.3 solar produces poorer fits. It is concluded that this effect is not due to any abundance gradient and probably due to cold gas clouds.

While the PSPC observation has confirmed the suggestion made by the SSS study of excess central absorption in A2199 (White et al. 1991), the magnitude of the column found by the PSPC (assuming a cooling flow model with no partial covering as used in the SSS analysis) is a factor of ten lower than that obtained from the SSS. This can be explained by the different energy bandpasses of the two instruments: the SSS operated over an energy range of 0.6-4.5 keV while the PSPC operated over the softer band of 0.1-2.0 keV. As the column density has the greatest effect on the x-ray spectrum below 0.6 keV, the PSPC should provide the most accurate measure of the column

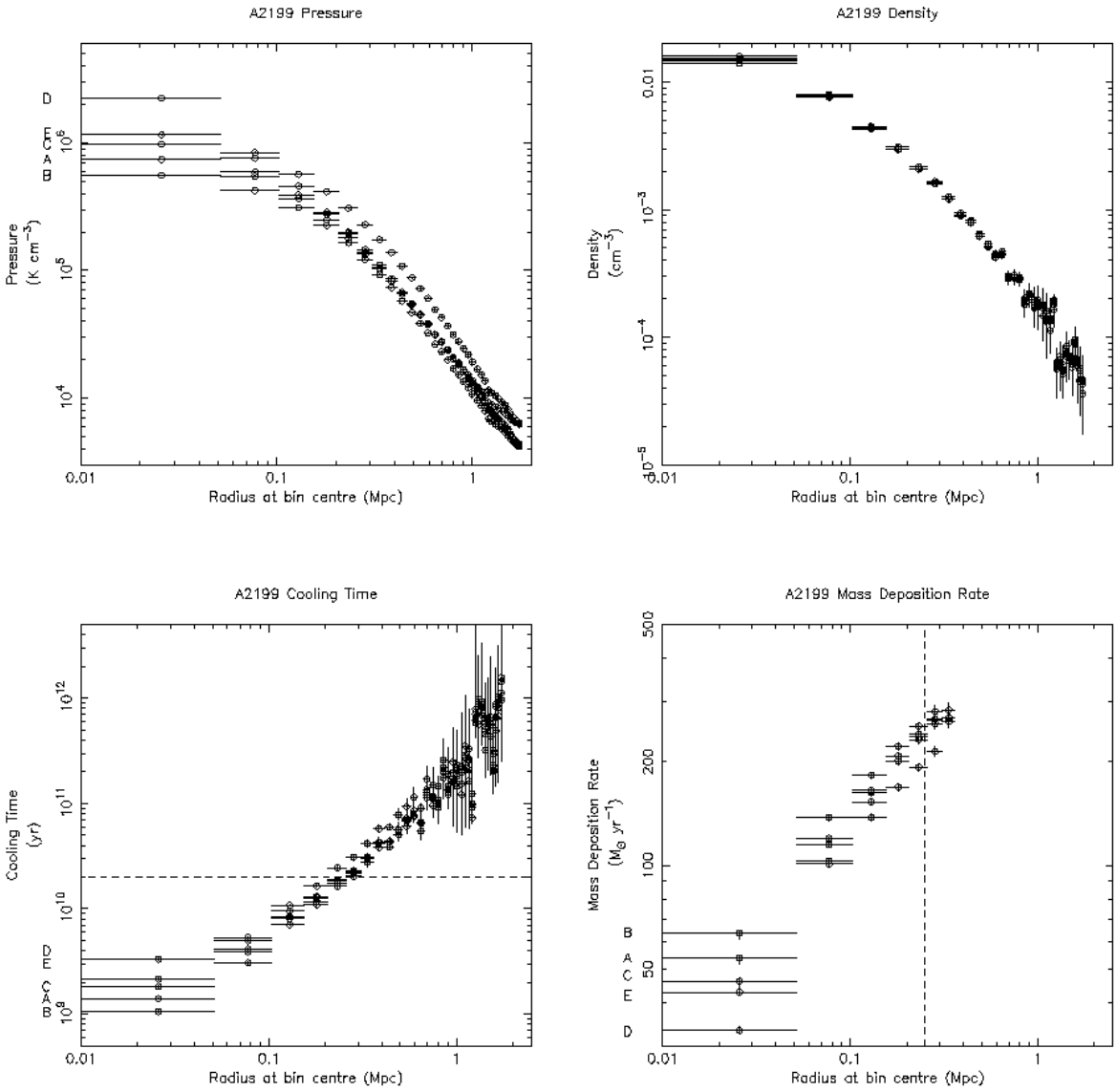

Fig. 12. The deprojected pressure, density, cooling time and $\dot{\mathrm{M}}$ profiles as a function of radius. The potentials are marked for the innermost bin. The dashed lines indicate cluster properties corresponding to a cooling time of 2×10^{10} years.

density. As shown in Sect. 3.2, inspection of the residuals of a fit to the data using a cooling flow model with the column density fixed at the SSS measurement shows an excess over the model for energies less than 0.6 keV. More detailed analysis showed that a partial covering model is required. A2199 exhibits a particularly low covering fraction and a correspondingly large intrinsic column density. It is intriguing to note that while the PSPC and SSS yield consistent results over similar energy ranges the errors in the SSS measurement for the column density do not accommodate the PSPC measurement. An underestimation of the column density by the PSPC due to, for example, poor background subtraction can almost certainly be ruled out as this would mean an underestimate of the column at larger radius, and hence a lower column than predicted by HI measurements. This may mean that the lower limit to the SSS measurements are overestimates. This could be caused by inaccurate modelling of the behaviour of ice deposited over the detector window, which can absorb x-rays to yield an equivalent absorbing column of 10^{20-21} cm^{-2} (White et al. 1991).

In conclusion, the PSPC measurements provide the most accurate measure and description of the central absorption in A2199. The absorption may be due to cold clouds deposited by the cooling flow. An estimate of the mass of these clouds was given in Eq. 3.4 . However, as the clouds are modelled as a sheet positioned in front of the cooling flow rather than embedded inside the flow, all of the cooling flow emission is effectively obscured by the sheet. This means that the intrinsic column and hence mass of cold gas estimated may be a lower limit; the true value may be up to 50 % higher and the mass of cold gas can be up to $\sim 10^{11}$ M$_\odot$.

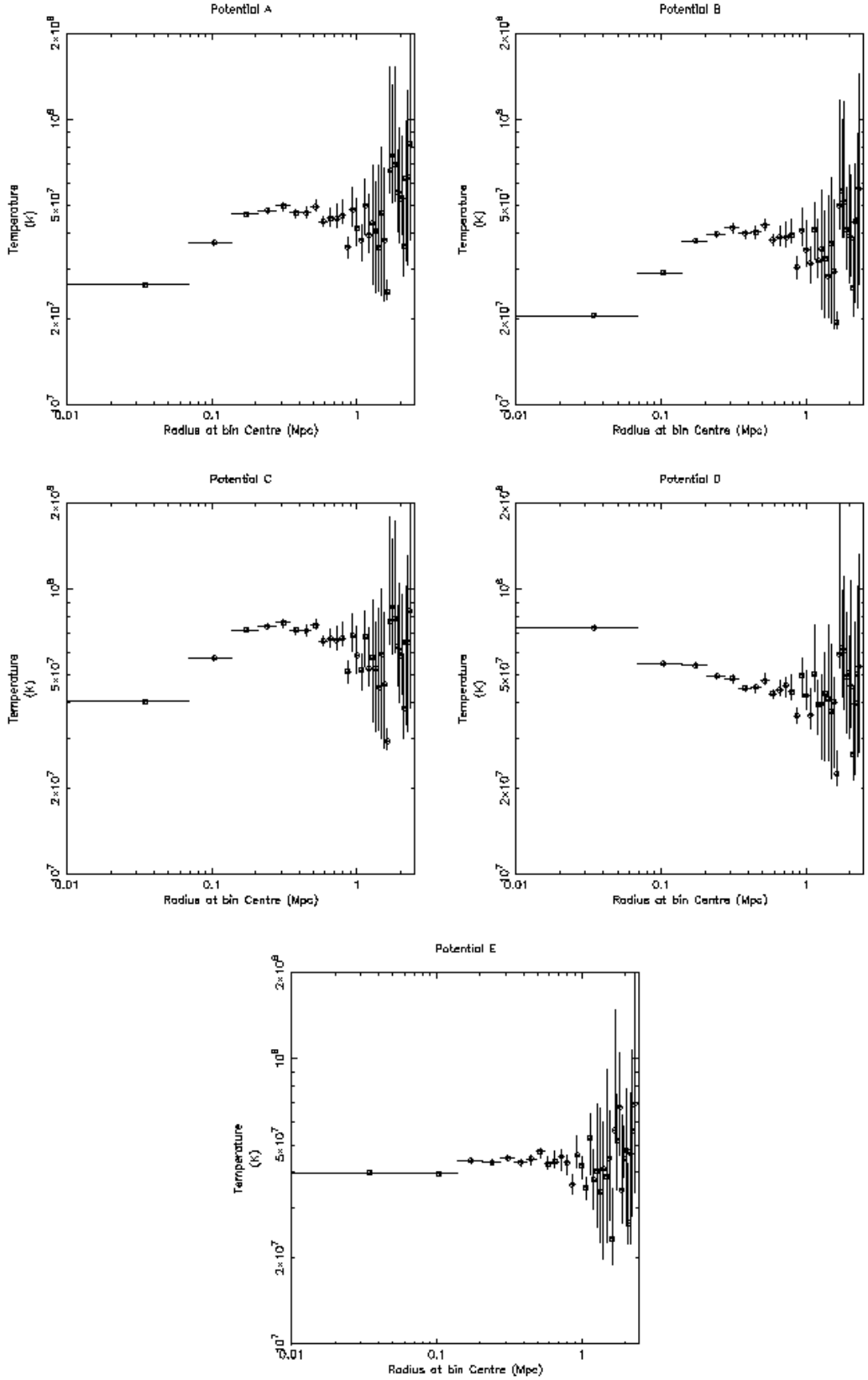

Fig. 13. The deprojected temperature profiles for each assumed potential.

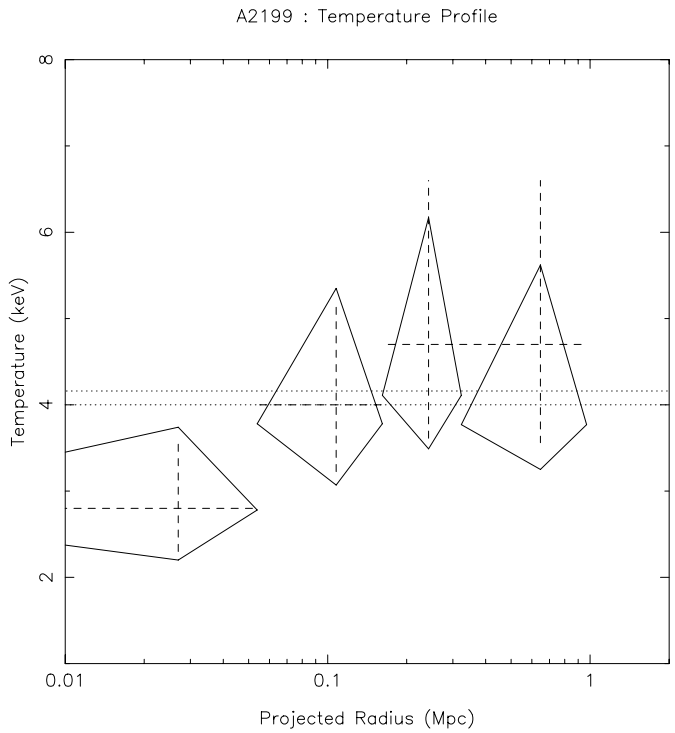

Fig. 14. The re-projected temperature profile (diamonds), superimposed on the observed temperature profile (crosses). The dotted lines represent the 90 % confidence limits to the Ginga large-beam measurement.

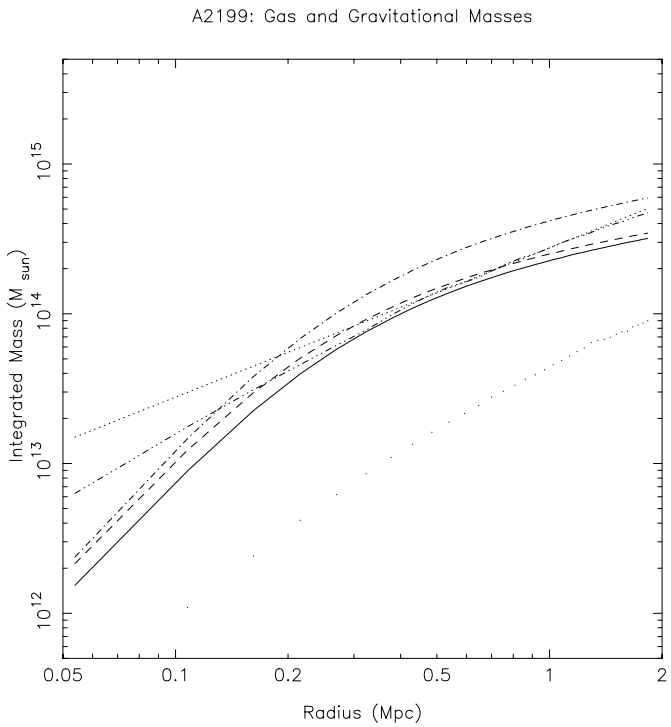

Fig. 15. The gas profile and constraints to the gravitational mass inferred from the deprojection analysis. The lowermost (dotted) curve represents the gas mass profile. The gravitational mass profiles are plotted as follows: Potential A (dashed), B (solid), C (dot-dashed) D (triple dot-dashed) and E (upper dotted line).

It is interesting to examine the evidence for cold gas in other wavebands. Searches for this putative gas based on CO observations have proved unsuccessful (Antonucci & Barvainis 1994; Bregman & Hogg 1988; Grabelsky & Ulmer 1990), and 21 cm observations have lead to an upper limit of $\sim 10^9$ $\mathrm{M}_\odot$ (McNamara & Jaffe 1994 and references therein), largely ruling out HI as a possible form for the cold gas. However, it has been postulated (Fabian et al. 1994) that dust forms in the cores of cooled gas clouds. This would mean that CO molecules freeze onto the grains, and hence avoid detection. Annis & Jewitt (1993) have measured an upper limit to the total dust mass within the central 10 kpc of A2199 of 6.8×10^7 $\mathrm{M}_\odot$ using $800 - 1100$ μm spectroscopy . This value is derived assuming that the mean temperature of the dust grains is approximately 20 K. Fabian et al. (1994) calculate a lower mean temperature of 10 K, which increases this limit by a factor of 3. Assuming a galactic gas-dust ratio of 157, this means an upper limit for the total gas mass is $\sim 3 \times 10^{10}$ $\mathrm{M}_\odot$ within the central 10 kpc, or roughly 1.2×10^{11} $\mathrm{M}_\odot$ out to a radius of 40 kpc (assuming $\dot{\mathrm{M}} \propto \mathrm{r}$). The mass of cold gas estimated from the spectral data is within this limit. Improved sub-millimetre observations will place strong constraints on the total dust mass and hence provide a strong test for this hypothesis.

The cold gas may have been introduced into the central regions by the cooling flow. Using a mass deposition rate of $\dot{\mathrm{M}} = 67$ $\mathrm{M}_\odot$ yr^{-1} and a cluster age of $\mathrm{t_a} = 2 \times 10^9$ yr gives a mass of 1.3×10^{11} $\mathrm{M}_\odot$ deposited by the cooling flow. This is a factor of greater than 2 higher than the amount of cold gas estimated, and so it is plausible that the cooling flow could introduce this cold material into the central regions of the cluster.

There is a strong body of evidence to suggest that the fate of the cold gas is in the form of low mass stars (Fabian 1991; O'Connell & McNamara 1989). Comparing the surface brightness profile of NGC 6166 with a range of test Initial Mass Functions (IMFs), Fabian (1991) has computed upper limits for a stellar population produced by a cooling flow. Using the mass deposition rate presented above, most stars will form with $\mathrm{M}_* < 1.5$ $\mathrm{M}_\odot$. Again, this value is much less if the cooling flow was stronger in the past.

It has been suggested (see e.g. Sarazin 1986) that cD galaxies may be the product of cooling flows. This stems from the fact that most cooling flow clusters contain central cDs. Minkowski (1961) finds NGC 6166 to be extended out to 68 kpc and estimates a blue luminosity for this galaxy of 3.8×10^{11} $\mathrm{L}_\odot$. Assuming a M/L ratio of 8 (David et al. 1990), this gives a galaxian mass of 3×10^{12} $\mathrm{M}_\odot$. The gas mass out to this radius from Fig. 15 is $\approx 5 \times 10^{11}$ $\mathrm{M}_\odot$. The total baryonic mass of NGC 6166 is then about 3.5×10^{12} $\mathrm{M}_\odot$. This is larger than the total mass predicted to have been deposited by the cooling flow, and suggests that an alternative process must take place to allow for the formation of cD galaxies, e.g. galaxy mergers or galactic cannibalism.

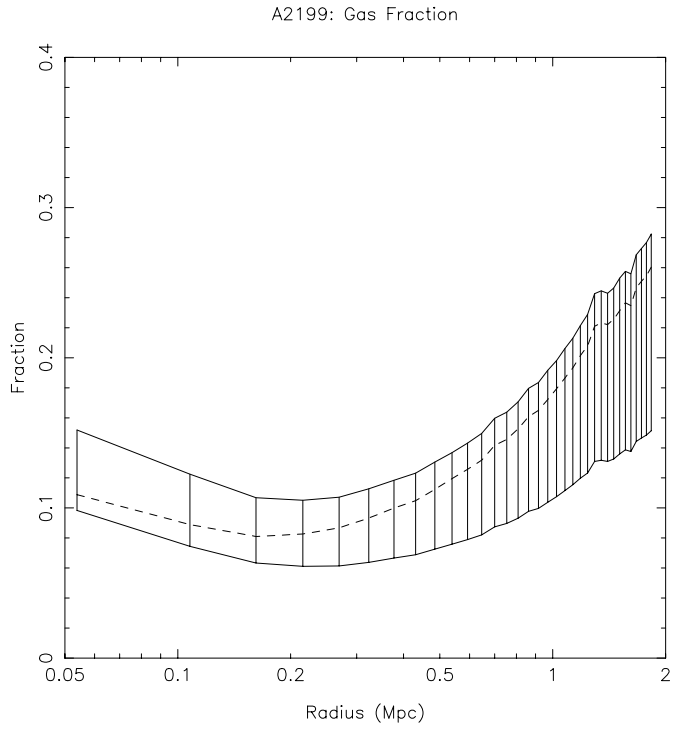

Fig. 16. The gas content in A2199 as a function of radius. At $1.8\ \mathrm{Mpc}$, the ratio is approximately 0.1-0.3 .

Further work to establish strong constraints on the mass deposition rate and the intrinsic absorption to the centre of the cluster would clarify this. Such constraints may be provided by high quality ASCA data, or in the next decade by AXAF or XMM missions.

5.3. The mass distribution

Combining the gas and total mass distributions presented, an estimate of the baryonic mass distribution is made. The allowed range in gravitational mass is judged from the range in gravitational profiles constrained by the spectral data, and a variety of gravitational models were investigated. It should be noted that all the allowed models fit within the extreme King potentials used, which flatten at large radii. However, alternative models, which are steeper at large radii but suitably flat at lower radii may also be allowed by the spectral data. Note that the apparent rise in the gas fraction at large radii may be a consequence of limitations in the gravitational models investigated. This effect has been seen in other cluster studies (e.g. Durret et al. 1994; Buote & Canizares 1996). Improved observations of A2199 using instruments with reasonable spectral and spatial capability will provide stronger model-independent constraints on the temperature and its gradient up to a radius of ~ 3 Mpc. Changing the form of the potential will have little effect at radii < 2 Mpc where spectral constraints on the gas temperature exist.

While there is still some uncertainty in the fraction of gas to total mass at large radii the gas fraction may indeed be increasing with radius. If so, the gas will be distributed with a larger scale length than the underlying dark matter.

The ratio of gas to total mass for A2199 is ~ 0.2 out to 2 Mpc, and the data suggest it to be increasing at larger radii (although as noted above this may be slightly model dependent and the possibility of a constant mass fraction cannot be completely ruled out). Similar baryonic fractions have been found in other rich clusters (e.g. White & Fabian 1995; Siddiqui 1995; White & Frenk 1991). This is a lower limit as some of the 'dark' matter may be baryonic. A crude estimate of the total galaxian mass of A2199 out to the same radius was made using Automated Photographic Measuring System (APM; Kibblewhite et al. 1983) scans of Palomar All Sky Survey Plates (Siddiqui 1995). This was found to be $2 \times 10^{13}\ M_{\odot}$, approximately 5 % of the total gravitational mass, and yields a observed baryonic fraction of about 0.25.

As the total cluster mass scales as approximately h_{50}^{-1} while the galaxy and gas masses scale as h_{50}^{-1} and $\mathrm{h}_{50}^{-5/2}$ respectively, then a lower limit to the baryonic fraction, $\mathrm{F_b}$, within $2\ \mathrm{Mpc}$ is

$$\mathrm{F_b} \geq \mathrm{M_b/M_{tot}} = 0.1 + 0.2\ \mathrm{h}_{50}^{-3/2} \quad (4)$$

where the first and second terms correspond to the galaxy and gas contributions respectively, assuming typical gas and galaxian fractions of the total cluster mass of 0.3 and 0.05 respectively.

The cosmological baryon fraction is given by $\Omega_{\mathrm{b}}/\Omega_0$, where Ω_{b} is the mean baryon density and Ω_0 is the mean density of all forms of matter. There is strong theoretical support for a flat ($\Omega_0 = 1$) universe. Standard cosmic nucleosynthesis predicts a baryon density Ω_{b} of $\approx 0.05\ \mathrm{h}_{50}^{-2}$ (Walker et al. 1991). The cosmological baryon fraction is then about $0.05\ \mathrm{h}_{50}^{-2}$ and is much less than that estimated for A2199. This discrepancy has been noted in a number of other rich clusters, e.g. Coma (White et al. 1993), A478 (White et al. 1994) and even in poor groups, e.g. HCG 62 (Ponman & Bertram 1993), NGC 5044 (David et al. 1994).

There are a number of means by which these two values can be accommodated (see White et al. 1993 for a detailed discussion). The obvious solution is that $\Omega_0 \approx 0.2$, ie less than the closure value. This is in conflict with standard inflationary models which require Ω_0 to be unity. Alternatively, baryons may be concentrated in centres of clusters and hence these measurements are overestimates of the cosmological fraction. However, the data presented here (and other observations) suggest an increase in the baryonic fraction with radius rather than the decrease which would be required. Furthermore, it is difficult to derive a mechanism (for example infall) which would introduce these baryons into the inner regions (White et al. 1993).

If this fraction is rising with radius, which is allowed by the data, then it is possible for matter at scales of $10\ \mathrm{Mpc}$ to be entirely baryonic. However, this would invoke another paradox: in a low density universe of wholly baryonic material, it is difficult to form any structure, as there is little time for the matter to depart from the flat primordial spectrum suggested from observations of the microwave background, e.g. COBE (Smoot et al. 1992).

Acknowledgements. H.S. acknowledges a research studentship from the Science and Engineering Research Council of the United Kingdom and use of the STARLINK facilities. Michael Dahlem is thanked for useful discussions.

References

Abell, G.O., Corwin, H.G., Olowin, R.P., 1989, ApJS 70, 1
Allen, S.W., Fabian, A.C., 1994, MNRAS 269, 409
Allen, S.W., Fabian, A.C., 1997, MNRAS 286, 583
Allen, S.W., Fabian, A.C., White, D.A., et al., 1993, MNRAS 262, 901
Annis, J., Jewitt, D., 1993, MNRAS 264, 593
Antonucci, R., Barvainis, R. 1994, AJ 107, 448
Bade, N., Engels, D., Fink, H. et al., 1992, A&A 254, L21
Bevington, P.R., Robinson, D.K., 1992, Data Reduction and Analysis for the Physical Sciences, McGraw-Hill
Bregman, J.E., Hogg, D.E., 1988, AJ 96, 455
Briel, U.G., Aschenbach, B., Hasinger, G., et al., 1996, ROSAT User's Handbook
Buote, D.A., Canizares, C.R., 1996, ApJ 457, 565
Butcher, J.A., 1994, Ph.D. thesis, University of Leicester
Cavaliere, A., Fusco-Femiano, R., 1976, A&A 49, 137
David, L.P., Arnaud, K.A., Forman, W., Jones, C., 1990, ApJ 356, 32
David, L.P., Forman, W., Jones, C., Daines, S., 1994, ApJ 428, 544
Davis, J. 1991, Starlink User Note 52
Dixon, K.L., Godwin, J.G., Peach, J.V., 1989, MNRAS 239, 257
Durret, F., Gerbal., D., Lachieze-Rey, M., et al., 1994, A&A 287, 733
Edge, A.C., 1989, Ph.D. thesis, University of Leicester
Edge, A.C., Stewart, G.C., 1991, MNRAS 252, 428
Fabian, A.C., 1991, A&AR 2, 191
Fabian, A.C., Hu, E.M., Cowie, L.L., Grindlay, J., 1981, ApJ 248, 47
Fabian, A.C., Johnstone, R.M., Daines, S.J., 1994, MNRAS 271, 737
Forman, W., Jones, C., Tucker, W., 1984, ApJ 277, 19
Gerbal, D., Durret, F., Lima-Neto, G., Lachieze-Rey, M., 1992, A&A 253, 77
Giommi, P., Tagliaferri, G., Beuermann, K., et al., 1991, ApJ 378, 77
Grabelsky, D.A., Ulmer, M.P., 1990, ApJ 355, 401
Gregory, S.A., Thompson, L.A., 1984, ApJ 286, 422
Jones, C., Forman, W., 1984, ApJ 276, 38
Kibblewithe, E.J., Bridgeland, M.T., Bunclark, P., Irwin, M.J., 1983, in D. Klinger-Smith (ed.), Proceedings of the Astronomy Micro-densitometry Conference, 1, III (AMC)
McNamara, B.R., Jaffe, W., 1994, A&A 281, 673
Minkowski, R., 1961, PASP 70, 143
Morrison, R., McCammon, D., 1983, ApJ 270, 119
O'Connell, R., McNamara, B., 1989, ApJ 98, 180
Pfeffermann, E., Briel, E., Hippmann, U.G., et al., 1987, The focal plane instrumentation of the ROSAT telescope. In: Proceedings of the International Society for Optical Engineering 733, 519
Plucinsky, P.P., Snowden, S.L., Briel, U.G., et al., 1993, ApJ 418, 519
Ponman, T.J., Bertram, D., 1993, Nature 363, 51
Porter, A.C., Schneider, D.P., Hoessel, J.G., 1991, AJ 101, 1561
Raymond, J.C., Smith, B.W., 1977, ApJS 35, 419
Sarazin, C.L. 1986, Rev. Mod. Phys. 58,1
Shefer, R.A., Haberl, F., Arnaud, K.A., Tennant, A.F., 1991, XSPEC: An X-Ray Spectral Fitting Package, ESA Publications, Noordwijk
Siddiqui, H.I., 1995, Ph.D. thesis, University of Leicester
Smoot, G.F., Bennett, C.L., Kogut, A., et al., 1992, ApJL 396, 1
Snowden, S.L., Plucinsky, P.P., Briel, U., et al. 1992, ApJ 393, 819
Stark, A.A., Gammie, C.F., Wilson, R.W., et al., 1992, ApJS 79, 77
Stewart, G.C., Fabian, A.C., Jones, C., Forman, W., 1984, ApJ 285, 1
Struble, M.F., Rood, H.J., 1991, ApJS 77, 363
Walker, T.P., Steigmann, G., Schramm, D.N., et al. 1991, ApJ 376, 51
Wells, A., Abbey, A.F., Barstow, M.A., et al., 1990, SPIE, 1344, 320
White, D.A., Fabian, A.C., 1995, MNRAS 273, 72
White, D.A., Fabian, A.C., Allen, S.W., et al. 1994, MNRAS 269, 589
White, D.A., Fabian, A.C., Johnstone, R.M., et al., 1991, MNRAS 252, 72
White, S.D.M., Frenk, C.S., 1991, ApJ 379, 52
White, S.D.M., Navarro, J.F., Evrad, A.E., Frenk, C.S., 1993, Nature 366, 429
Zabludoff, A.I., Huchra, J.P., Geller, M.J., 1990, ApJS 74, 1